

# Atom identification in bilayer moiré materials with Gomb-Net

Austin C. Houston<sup>1</sup>, Sumner B. Harris<sup>2\*</sup>, Hao Wang<sup>3</sup>, Yu-Chuan Lin<sup>4</sup>, David B. Geohegan<sup>1</sup>, Kai Xiao<sup>2</sup>, Gerd Duscher<sup>1\*</sup>

<sup>1</sup> Department of Materials Science and Engineering, University of Tennessee, Knoxville, TN 37996

<sup>2</sup> Center for Nanophase Materials Sciences, Oak Ridge National Laboratory, Oak Ridge, TN 37831

<sup>3</sup> Min H. Kao Department of Electrical Engineering and Computer Science, The University of Tennessee, Knoxville, Tennessee 37916, United States

<sup>4</sup> Department of Materials Science and Engineering, National Yang Ming Chiao Tung University, Hsinchu City, 300, Taiwan

\*Correspondence should be addressed to: [harrisb@ornl.gov](mailto:harrisb@ornl.gov) or [gduscher@utk.edu](mailto:gduscher@utk.edu)

## Abstract

Moiré patterns in van der Waals bilayer materials complicate the analysis of atomic-resolution images, hindering the atomic-scale insight typically attainable with scanning transmission electron microscopy. Here, we report a method to detect the positions and identity of atoms in each of the individual layers that compose bilayer heterostructures. We developed a deep learning model, Gomb-Net, which can distinguish atomic species in each individual layer, effectively deconvoluting the moiré pattern to enable layer-specific mapping of strain and dopant distributions, unlike other methods which struggle with moiré-induced complexity. Using this approach, we explored Se atom substitutional sites in a twisted fractional Janus  $\text{WS}_2\text{-WS}_{2(1-x)}\text{Se}_{2x}$  heterostructure and found that layer specific implantation sites are unaffected by the moiré pattern's local energetic or electronic modulation. This advancement enables atom-identification within material regimes where it was not possible before, opening new insights into previously inaccessible material physics.

Notice: This manuscript has been authored by UT-Battelle, LLC, under Contract No. DE-AC05-00OR22725 with the U.S. Department of Energy. The United States Government retains and the publisher, by accepting the article for publication, acknowledges that the United States Government retains a non-exclusive, paid-up, irrevocable, world-wide license to publish or reproduce the published form of this manuscript, or allow others to do so, for United States Government purposes. The Department of Energy will provide public access to these results of federally sponsored research in accordance with the DOE Public Access Plan ( <http://energy.gov/downloads/doe-public-access-plan> ).

## Introduction

Over the past decade, twisted van der Waals bilayers (TvdWBs) have drawn significant attention for their unique and often tunable properties, the promise for creating elusive states of matter, and studying the strongly correlated physics that emerge<sup>1</sup>. The moiré lattice created by two monolayers of graphene or transition metal dichalcogenides (TMDs) modulates electronic and topological properties on the nanoscale<sup>2</sup>, producing phenomena from perfect arrays of quantum emitters to excitonic superlattices with tunable, giant spin-orbit coupling<sup>3</sup>. In bilayer graphene, unconventional superconductivity emerges at a  $\sim 1.1^\circ$  “magic twist angle”, where the Fermi velocity drops to zero and energy bands become flat<sup>4</sup>.

Each atom in a monolayer of these types of materials is readily imaged with high-angle annular dark-field scanning transmission electron microscopy (HAADF-STEM), and is identified by the image contrast, which is roughly proportional to the square of the atomic number  $Z$ . Thus, any defect or distortion from the ideal crystal lattice is also directly identifiable. Microscopists have developed numerous traditional techniques for identifying atom positions and their species in the last half century. However, when these methods fail, deep learning models such as AtomAI<sup>5</sup> and AtomSegNet<sup>6</sup> are employed for atom finding, defect identification, strain mapping, and local structure analysis<sup>7-12</sup>. Neural networks like these are semantic segmentation models based on the U-Net<sup>13,14</sup> architecture and offer advantages such as improved accuracy in atom localization compared to traditional methods, with minimal parameter tuning, and rapid prediction generation within milliseconds<sup>6</sup>.

However, the moiré interference in HAADF-STEM images of TvdWBs introduces additional variations in image contrast due to the gradual change in atomic stacking through the superlattice, preventing atom identification with modern image analysis methods. Although

Fourier filtering can estimate the repeating atomic lattices, it discards information about inhomogeneities and atomic species. This local insensitivity is particularly significant because strain and defect engineering can have a significant effect on TvdWBs properties<sup>15</sup>. While vacancies in 2D materials are often degenerative, some novel optical properties are enabled by their presence<sup>16,17</sup>, such as point defects in WSe<sub>2</sub> monolayers acting as single photon emitters<sup>18</sup>. It is clear; the location, quantity, and local structure of point defects in these systems determines their properties. Although multi-slice ptychography can identify atoms in moiré materials, this technique is computationally intensive, requires parameter optimization, expensive equipment, and significant expertise. Identification of atomic species in TvdWBs from HAADF-STEM images remains a challenge that must be addressed to gain a deeper understanding of how the local atomic structure of moiré materials affects their properties.

Here, we develop a deep learning model, called Gomb-Net (groupwise combinatorial multi-branch U-Net), that is capable of localizing and identifying atoms in each individual layer of TvdWBs, enabling us to probe the local atomic structure of these moiré materials. Gomb-Net uses a multi-branch decoder U-Net architecture that performs image segmentation on HAADF-STEM images to effectively deconvolute the individual monolayers from the moiré pattern to reveal layer-wise distributions of dopant atoms, defects, or strain. We demonstrate superior performance compared to the conventional U-Net architecture for this task with images from two TvdWBs test cases: twisted bilayer graphene (TBG) and a twisted TMD heterostructure of WS<sub>2</sub>-WS<sub>2(1-x)</sub>Se<sub>2x</sub>. Gomb-Net can be trained in minutes on modern personal computers and generates predictions in milliseconds, making advanced analysis of moiré matter widely accessible and ideal for real-time atom identification and analysis during automated or autonomous STEM experimentation.

## Results

### *Simulated Twisted Bilayer Graphene*

The TBG system, being one of the simplest and yet most impactful moiré systems, serves as the ideal case for testing the basic capabilities of Gomb-Net against other atom finding techniques. We start by generating a simulated dataset of TBG and train several models. One simulated HAADF-STEM image of TBG at atomic resolution (**Fig 1a**) shows repeating moiré unit cells, where atom identification seems feasible at the highly symmetric AA stacking centers. However, as we move away from the clearly defined carbon rings into intermediate stacking regions, the moiré pattern complicates the interpretation of the  $Z$  contrast - for the human eye, as well as for traditional atom-finding methods. Thus, we developed Gomb-Net to accurately identify the positions of atoms in each of the individual layers to deconvolute the moiré pattern for atomic scale analysis.

Gomb-Net achieves through two modifications to the standard U-Net model. First, we employ a physics-informed loss function during training, which we call the groupwise combinatorial loss (Gomb-Loss, detailed in the Methods section). This loss function disregards the layer ordering (physically, which layer is on top of the other does not affect HAADF-STEM image formation), in favor of the sorting the atoms into individual layers. Mathematically, Gomb-Loss prioritizes interlayer coherence and considers multiple stacking order scenarios through a series of grouping outputs and averaging reciprocals, similar to a harmonic mean. Gomb-Net is trained on simulated HAADF-STEM images of the TvdWB system of interest, TBG in this first example. Thus, the performance and limitations of Gomb-Net are also critically influenced by the quality and diversity of the simulated datasets used for training, and their resemblance to real-world datasets. Detailed descriptions of the training data generation are included in the Methods section

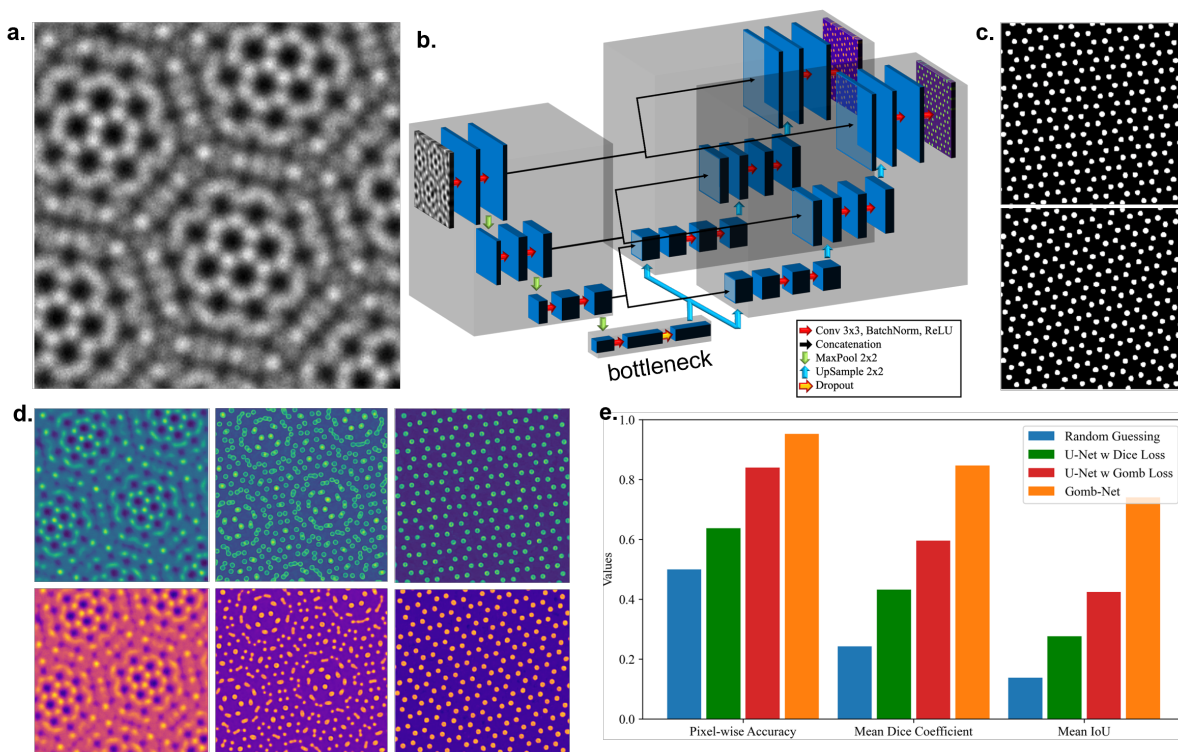


**Fig. 1 | Atom-finding in Moiré lattices is enabled by Gomb-Net.** **a**, Simulated STEM Z-contrast test image of atomically resolved TBG, used as network input (not seen during training). **b**, Schematic of the network architecture with a single encoder before the bottleneck layer, and two separate decoders after the bottleneck layer. Skip connections (black) help preserve fine detail. **c**, Binary images showing the two layers of carbon atom positions derived from the input. **d**, Raw network outputs of test image for regular U-Net (left), U-Net with the groupwise, combinatorial loss function (middle), and Gomb-Net (right). **e**, Performance comparison of different networks on a test dataset of 800 images across accuracy metrics.

and Supplemental Information with the code and data provided online. The second technical development of Gomb-Net is the adoption of a multi-branch U-Net architecture, shown in **Fig 1b**. Other U-nets used for semantic segmentation typically have only one decoder after the bottleneck layer, which is responsible for producing all the output layers of the network. The multi-branch architecture of Gomb-Net allows for multiple decoders, each responsible for segmenting a single atomic layer (the two decoders in this example are visible in **Fig 1b, right**). This dual-decoder architecture has been used for multi-task learning on biological data<sup>19</sup> and we adapt it here for segmentation of HAADF-STEM images of TvdWBs. After training, Gomb-Net produces pixel

wise classifications of the atom locations and identity in each layer of the bilayer heterostructure (**Fig 1c**) which can be used to analyze the strain, defects, and composition of TvdWBs.

To show the necessity of these technical developments, the raw outputs of three networks are shown (**Fig 1d**) from left to right, standard U-Net, U-Net with Gomb-loss, and Gomb-Net with Gomb-loss. On the left, the network predictions naively classify by pixel brightness. In the middle, the introduction of Gomb-loss localizes the atom predictions, although both network outputs are still identical. On the right, multi-branch architecture leads to branch specialization, where individual atoms are identifiable in each separate layer. To evaluate network performance, we compare random guessing, U-Net, U-Net with Gomb-loss, and Gomb-Net with Gomb-loss across accuracy metrics for a test dataset of 800 simulated images (**Fig 1e**). Gomb-Net achieves pixel-wise accuracy of 0.98 on the test dataset while the U-Nets reach 0.86 with Gomb loss and 0.63 with Dice loss (the current standard for image segmentation tasks with U-Nets). The mean Intersection over Union (IOU) reveals Gomb-Net's advantage with 0.74 IOU, compared to 0.39 for U-Net with Gomb loss and 0.27 for U-Net with Dice loss, highlighting its superior performance in minimizing false positives and negatives. Accurately identifying atom positions while minimizing both false positives and false negatives is essential, as incorrect predictions can have significant implications for the structural analysis of materials.

### *Experimental Twisted Bilayer Graphene*

Next, we demonstrate the performance of Gomb-Net on real HAADF-STEM images of twisted bilayer graphene. **Fig 2a** shows an experimental image of a twisted bilayer graphene sample twisted at  $\sim 26$  degrees, exhibiting a moiré pattern which makes identifying precise locations of individual C atoms challenging via traditional methods. This image is passed to the

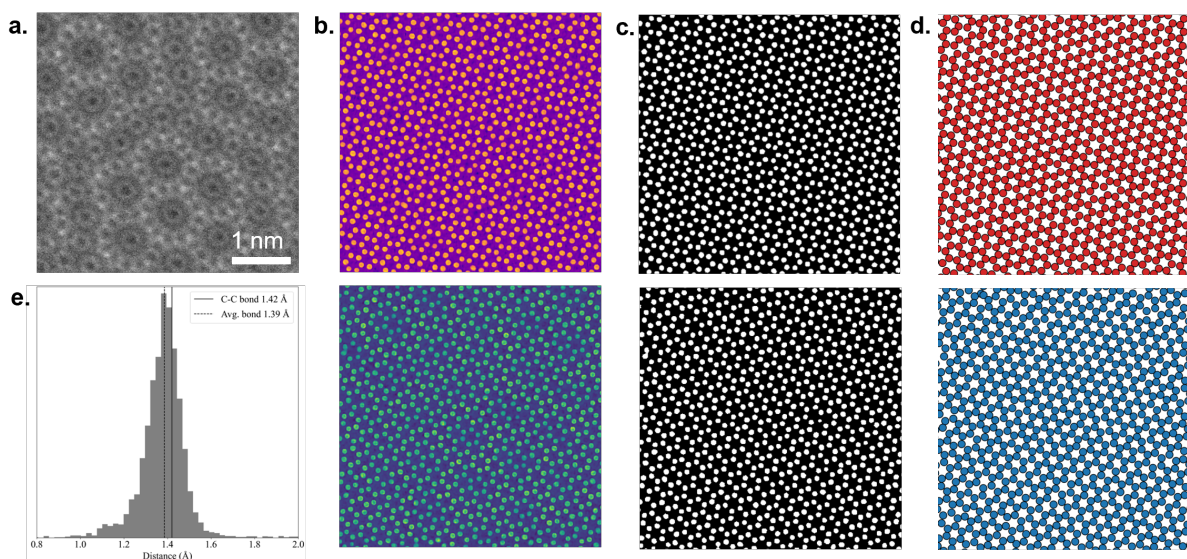


**Fig. 2 | Atom-finding in twisted bilayer graphene provides sub-pixel accuracy for carbon atoms in each layer.** **a**, Experimental STEM Z-contrast image of atomically resolved twisted bilayer graphene. **b**, Raw Gomb-Net outputs. **c**, Binarization of the outputs, with gating applied at threshold zero. **d**, Atom positions of both graphene layers, extracted from the binary images. **e**, Distribution of atom-atom bond distances for validation to a known physical value.

pre-trained Gomb-Net, which outputs confident predictions for atomic positions in each layer (**Fig 2b**). A threshold is applied at 0 to extract gated outputs (**Fig 2c**) which are translated into atomic coordinates via blob finding and computing the center-of-mass of each blob (**Fig 2d**), providing sub-pixel accuracy. To validate the network predictions, we calculate the C-C distance for all the identified atoms in both layers and compare to the known ideal C-C bond distance in bilayer graphene ( $1.42 \text{ \AA}$ )<sup>20</sup>. **Fig 2e** shows a histogram of predicted C-C distances with the mean value of  $1.39 \text{ \AA}$  and full width half max (FWHM)  $0.12 \text{ \AA}$ , which gives a 2.11% difference from the anticipated value and is well within the experimental uncertainty, especially knowing that TBG exhibits hetero-strains over 0.2 % across different regions of the moiré<sup>21</sup>. We achieve pixelwise precision in this measurement since the resolution of a  $256 \times 256$  is  $\sim 0.11 \text{ \AA}/\text{pixel}$ . We repeated this procedure with several experimental images with similar success.

### *Twisted $WS_2$ - $WS_{2(1-x)}Se_{2x}$ bilayers*

Next, we apply Gomb-Net to a more complicated case of twisted bilayer TMDs. These types of TvdWB structures are particularly promising for producing tunable moiré matter to control interlayer excitons<sup>22</sup>. We examine the case of an alloy bilayer heterostructure, where the moiré pattern is complicated by both twist angle and a difference in lattice constant. Specifically, we examine a twisted  $WS_2$ - $WS_2$  bilayer where the Se atoms have been preferentially implanted into the S sites on the outermost exposed chalcogen sublayer to form a fractional Janus alloy<sup>23</sup>. A fractional Janus layer is formed at the stoichiometry  $x < 0.5$  and a full Janus WSSe layer is formed at the stoichiometry  $x = 0.5$ <sup>24</sup> (**Fig 3g**). We refer to the resulting TvdWB as  $WS_2$ - $WS_{2(1-x)}Se_{2x}$ . Janus TMDs are interesting due to their intrinsic asymmetry which leads to a built-in electronic dipole and offers optical and catalytic properties that are different from the parent TMDs<sup>25</sup>, whose modulation by moiré patterns is largely unknown. Moreover, open questions remain about how strain, moiré patterns, and local structure may influence the doping/substitutional site preferences during the implantation process<sup>26</sup>.

Gomb-Net is necessary to answer the following question: does the modulated local coupling of the TMD layers induced by the moiré pattern significantly influence the implantation site probability of Se into the exposed TMD layer? This relationship can be elucidated from HAADF-STEM imaging experiments of these twisted  $WS_2$ - $WS_{2(1-x)}Se_{2x}$  structures, but analysis is significantly more complicated than in the bilayer graphene case. Graphene segmentation required identification of only 2 classes ( $C_A$  and  $C_B$ ), while this case requires 6 classes: W atoms, S-S columns, and Se-S columns in both monolayers (A, B). This case is further complicated by a continuum of overlap between atomic species and defects in the moiré pattern. This results in a broad distribution of Z-contrasts that are difficult to assign through traditional methods. If Gomb-

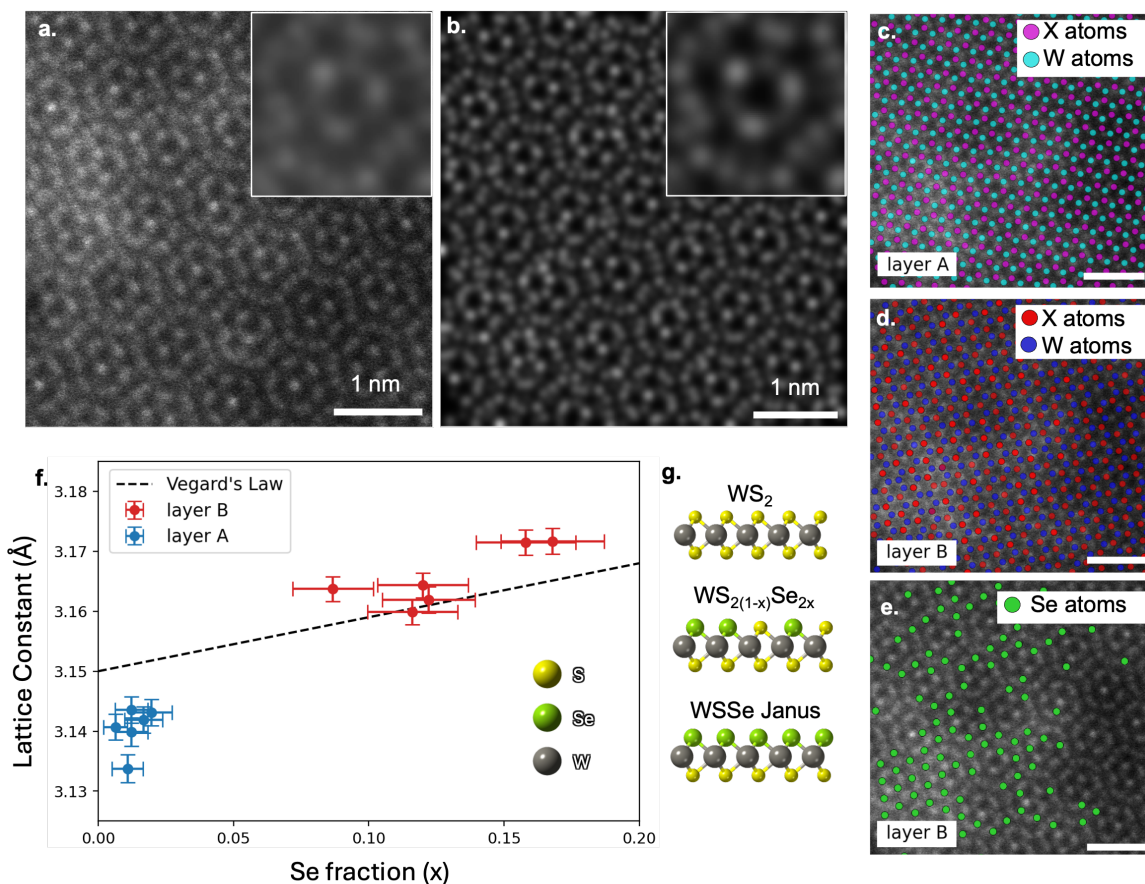


**Fig. 3 | Atom-finding in twisted  $WS_2$ - $WS_{2(1-x)}Se_{2x}$  bilayers confirms layer-selective Se substitution.** **a**, Atomically resolved HAADF-STEM image of the twisted  $WS_2$ - $WS_{2(1-x)}Se_{2x}$  heterostructure input to Gomb-Net. **b**, Simulated reconstruction image from Gomb-Net atomic position predictions. Insets: magnified regions for comparison. **c**, Tungsten and chalcogen atom positions found in layer A. **d**, Tungsten and chalcogen atom positions found in layer B. **e**, Distribution of all Se atoms in layer B. **f**, Lattice constant as a function of stoichiometry, calculated from the Gomb-Net outputs of 6 images. **g**, Atomic models of  $WS_{2(1-x)}Se_{2x}$  components for Vegard's law calculation in **f**.

Net can identify atoms and defects in this system, it will provide a better understanding of the mechanisms of Se implantation and the effects of local defects and strain on the structure and properties of twisted TMD alloy bilayers.

We synthesized a fractional Janus  $WS_2$ - $WS_{2(1-x)}Se_{2x}$  bilayer sample using pulsed laser deposition (PLD). In this process, a  $WS_2$  bilayer is exposed to the PLD plasma plume produced by ablating a solid Se target. The plume is composed of Se atoms and molecular clusters with a

maximum kinetic energy controlled to  $\sim 8.5$  eV/atom (see Methods for details). Previous experiments with WS<sub>2</sub> monolayers, using in situ Raman spectroscopy and ex situ STEM imaging, found that Se atoms are initially implanted primarily in the topmost chalcogen sublayer of WS<sub>2</sub>. The selenization then proceeds predominantly in a layer-by-layer<sup>24</sup> fashion until the WS<sub>2</sub> monolayer is fully converted to WSe<sub>2</sub><sup>24</sup>.

Gomb-Net analyzes a HAADF-STEM image of the fractional Janus alloy (**Fig 3a**) and extracts two sets of atomic positions and types, which are used to reconstruct a simulated HAADF-STEM image (**Fig 3b**). The reconstructed image serves as a visual method to confirm network performance on experimental data, where the ground truth is not known. The reconstructed image agrees remarkably well with the raw image, as shown in the insets featuring a high-symmetry region in the moiré lattice. Another region is shown in **Fig 3c-e**, where Se-S columns are present in one layer (**Fig 3d-e**) but absent in the other layer (**Fig 3c**). Across six similar regions, 98 % of all Se atoms (identified by the presence of Se-S columns) were found on the WS<sub>2</sub> layer exposed to the Se PLD plume. This is consistent with the previous experimental observations<sup>24</sup>. The atomic coordinates derived from model predictions for the six cropped regions are used to measure the lattice constant and stoichiometry of the individual layers. We can compare this ratio to Vegard's law, which states that the lattice parameter of a system with two constituents is approximately a weighted sum of the two constituents' lattice parameters. The change in lattice parameter as a function of stoichiometry follows Vegard's law, shown in **Fig 3f**. Notably, the lattice parameter of layer A corresponds to  $\sim 2$  % Se substitution, which agrees with the direct atom counting above.

With Se positions known, determination of whether the Se is preferentially substituted in the moiré lattice depends on labeling the different moiré sites. We approach this by first calculating

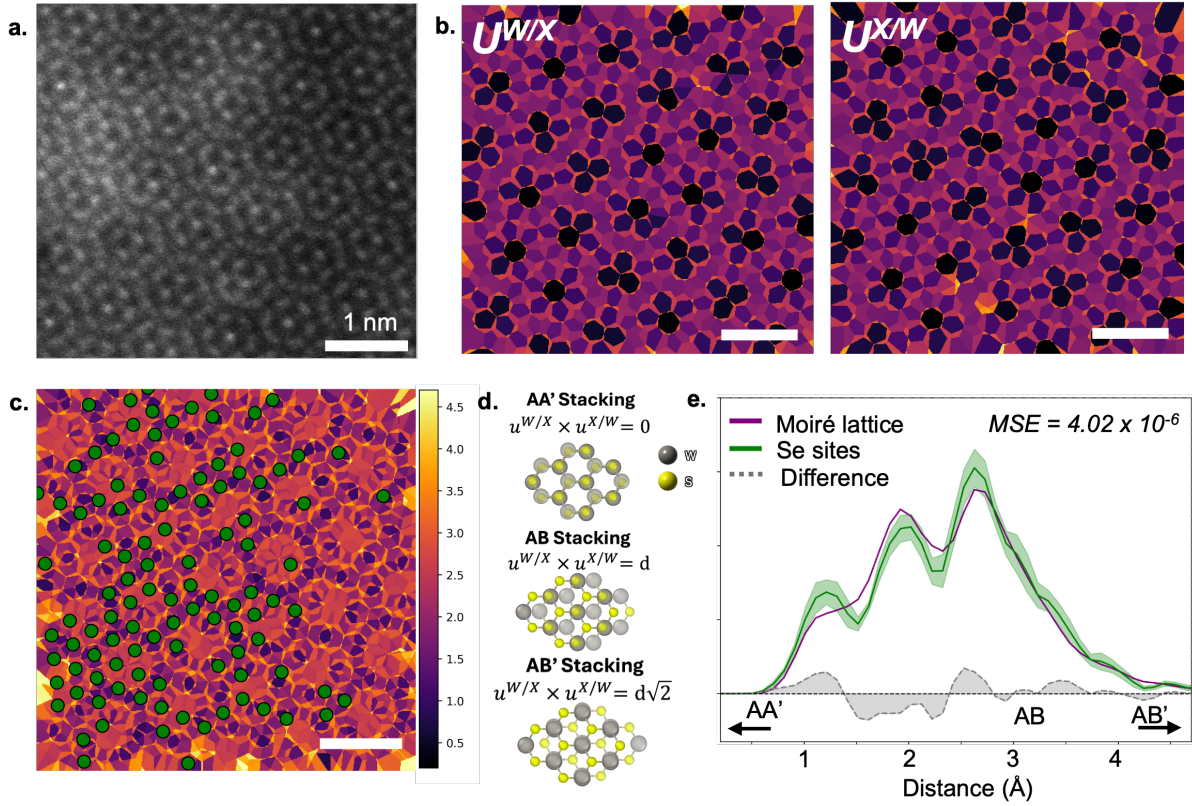


**Fig. 4 | Mapping the Se site distribution shows no preferential substitutional sites related to the moiré lattice.** **a**, Atomically resolved Z-contrast STEM image of a twisted  $\text{WS}_2\text{-WS}_{2(1-x)}\text{Se}_{2x}$  heterostructure. **b**, Order parameter maps calculated from Gomb-Net outputs. Left:  $U^{W/X}$ , the in-plane distance from layer A tungsten to the nearest layer B chalcogen column. Right:  $U^{X/W}$ , the in-plane distance from layer A chalcogen column to the nearest layer B tungsten. **c**, Local stacking order, calculated by  $U^{W/X} \times U^{X/W}$ , with Se-S columns (green). **d**, Schematic of local stacking order configurations and their respective values in terms of lattice parameter,  $d$ . **e**, Distributions of local stacking order in the moiré lattice (purple) and Se site occupancy (green) shows no preferential sites for Se substitution.

the order parameter vector<sup>27</sup>,  $u^{A/B}$ , which represents the the x-y projection distance between atoms in layer A and layer B. For each pixel in the image (**Fig 4a**), the nearest tungsten (W) and chalcogen columns (X) are identified, and the distance between them is calculated. Maps of the order parameters  $u^{W/X}$  and  $u^{X/W}$  are shown in **Fig 4b-c**. To produce a map of moiré stacking, we take the Euclidean norm of  $u^{W/X}$  and  $u^{X/W}$ . The resulting local stacking order map (**Fig 4c**), or moiré map, shows that a region with perfect AB stacking has a value of 0, a region with perfect AA'

stacking corresponds to the lattice parameter,  $d$ , and a region with perfect A'B stacking corresponds to  $d\sqrt{2}$  (**Fig 4d**). Since the lattice parameter changes with Se concentration (**Fig 3f**), we use the average value of 3.15 Å.

The final step to determine preferential occupation of the moiré lattice is to associate each Se-S column with the nearest moiré map value. This is done for six cropped regions of the original HAADF-STEM image, and the resulting distributions are shown in **Fig. 4e**. To estimate the probability density function of this distribution, we used Kernel Density Estimation (KDE) with a Gaussian kernel (details given in Methods). The KDE of the 1.3 million moiré sites is shown in purple, while the KDE of the 333 Se-S column positions found across the images is shown in green. The mean KDE of each distribution is plotted as a solid line, with plus/minus one standard deviation shown as the shaded region in **Fig. 4e**. Notably, the standard deviation of the moiré distance KDE is too small to be visible at this scale. The moiré distance KDE largely overlaps within one standard deviation of the Se-site KDE. Based on this data, the distribution of Se-sites follows that of the available moiré sites, indicating no preferential occupation of Se in the moiré lattice. The mean squared error between these two density-normalized distributions is  $4.02 \times 10^{-6}$ , indicating the distributions are similar.

## Discussion

Understanding the atomic-scale structure in each individual layer of a moiré heterostructure is of critical importance to correlate the local strain, defect, and dopant distributions with the unique electronic properties they provide, but their complex geometry prevents localization and identification of atoms in HAADF-STEM datasets using modern analysis methods. The deep learning model we developed and its physics informed training (Gomb-Net) enable us to extract

the atomic-scale structure of individual layers that compose twisted van der Waals bilayer materials from HAADF-STEM images, which was not possible before.

Application of this model to the case of twisted fractional Janus  $\text{WS}_2\text{-WS}_{2(1-x)}\text{Se}_{2x}$  heterostructures created by PLD implantation suggests the previous conclusion that selenization occurs predominantly layer-by-layer in a single monolayer of  $\text{WS}_2$ <sup>24</sup> is extensible to the bilayer  $\text{WS}_2$  case as well. Further, implantation into the exposed layer is independent of any local energetic or electronic modulations in the bilayer caused by the moiré pattern, at least in the  $\sim 8.5$  eV/atom implantation kinetic energy regime. It is possible that other twist angles or implantation kinetic energies could induce preferential implantation, but the difference in the energy threshold for implantation across this moiré is small compared to the energy of the incident Se plume in this case and therefore, the Se atoms implant randomly across the exposed layer.

Another critical finding is that a fraction of the chalcogen sites on the bottom layer ( $\sim 2$  % in this case) are implanted with Se atoms before the primary exposed layer is fully converted to Janus  $\text{WSSe}$  or  $\text{WSe}_2$ . When the model predicts on simulated images from the test dataset for cases where Se atoms are known to exist in only one layer, it falsely predicts Se atoms in the other layer with an error rate on the order of 0.5 %. Thus, it is likely that some of these Se atoms are false positives, while others are real. Regardless, these errors are still low enough to make statistically accurate statements about implantation as a function of local order and that the selenization still proceeds predominantly layer-by-layer; however, it suggests that a minority fraction of Se atoms penetrate through the top monolayer, as anticipated with this implantation kinetic energy. The analysis enabled by Gomb-Net opens opportunities to study the full range of implantation conditions and outcomes to reveal the mechanisms of Se implantation into bilayer TMDs by PLD.

Gomb-Net was built with the intention that scientists working with atomically resolved images of moiré materials can adapt the methodology to their own problems. The code is modular and flexible, with full control of hidden layers, loss function, output layers, and other hyperparameters, and was made to be adaptable to any moiré problem. The case of twisted  $\text{WS}_2\text{-WS}_{2(1-x)}\text{Se}_{2x}$  bilayer atom identification requires 6 output classes and the network performs well. Cases with  $> 6$  output classes or additional layers, such as a three-layer moiré material, are feasible by incorporating more decoder branches and adding additional terms to the loss function but have not been assessed yet. The key factor and limitation to Gomb-Net's performance, like with any supervised learning model, is the degree of similarity between the training dataset and the real experimental data. For example, if the goal is to identify lateral grain boundary structures in bilayer stacks of 2D materials, the training data must be constructed with simulated data that includes a variety of anticipated structures, likely determined by density functional theory or molecular dynamics simulations.

To summarize, the development and application of Gomb-Net enables the full array of analyses already developed by microscopists for atomically resolved datasets of TvdWBs, as well as enables new analyses unique to these material systems, such as experimental moiré mapping using interlayer order parameters. Additionally, Gomb-Net can be run efficiently on modern personal computers, making advanced analysis of moiré materials accessible and ideal for real-time analysis during autonomous STEM experimentation. These analyses are becoming critically important as the field expands into two extremes: pristine wafer-sized device fabrication and atomistically complex defect-engineered phases.

## Methods

### *Data Generation*

Gomb-Net is trained on separate sets of simulated HAADF-STEM images for the graphene (2000 images) and TMD bilayer (8000 images) cases, split into training, validation, and test subsets with proportions of 70%, 20%, and 10%, respectively. To generate our simulated HAADF-STEM images, we first generate the crystal structure for each bilayer scenario with atomic simulation environment package<sup>28</sup> and use a gaussian to approximate the scattering potential at each atomic position. This scattering potential is convoluted with a point spread function that represents the ideal case of a well-focused and aberration corrected electron probe, an airy disk, to generate the simulated Z contrast image. We include variations in layer twist angle, crystal rotation, atomic vacancy count, atomic vibration, atomic size, number of holes, hole and edge boundaries, and relative magnification. Poisson noise is randomly added to simulated images to replicate the stochastic nature of electron counting in actual HAADF imaging experiments. Large-scale gaussian noise is randomly added to approximate intensity variations caused by contamination on the sample. Images for the  $WS_2$ - $WS_{2(1-x)}Se_{2x}$  dataset are generated from a  $WS_2$  bilayer where S atoms are randomly replaced with Se according to one of the following randomly chosen scenarios: pristine (no Se substitution), single chalcogen sub-layer substitution, single crystal layer substitution, or substitution into both layers. This complexity in training data prepares the network for most S-Se substitution scenarios. The full range of varied parameters is shown in Table S1 and the process is visualized in Figure S1. The code used to generate the training data is available online: <https://github.com/ahoust17/DataGenSTEM.git>.

### *Network architecture and training*

The encoder is comprised of sequential convolution blocks, each containing two 2D convolutions with a (3x3) kernel using padding and stride of 1, ReLU<sup>29</sup> activation functions, and a 2D max pooling layer with a (2x2) kernel with stride of 2 for down-sampling. The first encoder block has 32 filters, and each sequential block doubles the number used in the previous block up to a maximum of 256 and 512 for the graphene and TMD models, respectively. Notably, there is a dropout layer in the bottleneck, with dropout set to 0.2 or 0.423 for the graphene and TMD models respectively, as we found this greatly improved generalization. The decoder legs are identical and are the reverse of the encoder, using 2D transpose convolutions for up-sampling. Skip connections are made by concatenating the output of each encoder block with the input of the appropriate decoder block. We used the Adam optimizer<sup>30</sup> for training and tuned the hyperparameters for the TMD model only using Ray Tune<sup>31</sup> with the Optuna search algorithm<sup>32</sup>. The full range of hyperparameters used for all models are available in Table S2.

### *Loss Function*

Choosing an appropriate loss function is crucial in training neural networks because it measures the discrepancy between predicted outputs and actual targets, guiding the network to adjust its weights to optimize performance for the specific task. For example, the Dice coefficient loss is highly effective for image segmentation tasks due to its ability to measure the overlap between predicted and actual segmentations, making it ideal for applications like medical image analysis<sup>33</sup>.

Gomb-Net implements a physics-informed loss function. Because HAADF images are 2D projections of 3D objects, under the kinematic scattering approximation, the atomic ordering in the out-of-plane dimension has no effect on the final image contrast, which is especially true for moiré bilayer systems. Thus, imposing a fixed layer ordering on the network's predictions

introduces unnecessary constraints that can hinder its performance. Therefore, a conventional loss function that enforces such an order is not suitable for our task. To address this, we implement a new groupwise combinatorial loss function (Gomb Loss), given by **Eq 1**:

$$\begin{aligned}
 & \textit{TotalLoss} \\
 &= \frac{1}{N} \sum_{i=1}^N \frac{\left( \text{DL}(T_{i,A}, T_{i,B}) - \text{DL}(O_{i,A}, O_{i,B}) \right)^2}{\left( \text{DL}(O_{i,A}, T_{i,A}) + \text{DL}(O_{i,B}, T_{i,B}) + \varepsilon \right)^{-1} + \left( \text{DL}(O_{i,A}, T_{i,B}) + \text{DL}(O_{i,B}, T_{i,A}) + \varepsilon \right)^{-1} + \varepsilon} \quad (1)
 \end{aligned}$$

where  $\text{DL}(\cdot)$  is a Dice loss calculated between the targets  $T$  and the model outputs  $O$  for class  $i$  in layer A or B,  $N$  is the number of classes, and  $\varepsilon$  is a small value to prevent division by zero set to  $1 \times 10^{-6}$ . The Dice loss is weighted to penalize false positives. Groupwise refers to the grouping together of the network outputs according to their branch (A or B in this case). This introduces a constraint indicating to the network that different atomic species in the same layer will be strongly correlated to each other. Combinatorial refers to the loss calculation between every combination of these output groups and target groups. This approach disregards the ordering of the outputs, focusing instead on the interlayer coherence and correspondence to the targets.

To achieve this mathematically, two combinatorial loss scenarios are considered. In one scenario, the network output matches the arbitrary mask ordering (left term in the denominator). In the other scenario, the output matches the inverse mask ordering (right term in the denominator). Because only one scenario is true at a time, one loss is small, and the other is large. To weight the scenario with the smaller loss, we take the harmonic mean for the losses of every scenario. Because this function is Schur-concave, its output will always be between the minimum loss and  $n \times$  the minimum loss (in this case,  $n = 2$ ). The output of this function is close to the loss of the correct ordering scenario, with a small contribution from the incorrect scenario and the stabilizing constant  $\varepsilon$ . This small contribution decreases as the network trains.

The loss values between the output and targets are computed with a modified Dice coefficient loss, which penalizes false positive guesses. The purpose of the numerator term is to discourage the network from predicting the same output from each branch, even in cases where the targets for each layer are similar. Before the introduction of this term, the network was predicting the same output for both layers consistently. It is possible that this loss function can be improved, modified, and even applied to problems in other fields that involve a non-specific ordering of grouped network outputs.

### *HAADF-STEM Imaging*

HAADF-STEM images of graphene and TMD bilayers were captured on a monochromated, probe corrected Thermofisher Scientific Spectra 300 operating at 60 kV accelerating voltage with a convergence angle of 30 mrad and a nominal screen current of 100 pA. The collection angle for the samples differed, with 80-200 mrad for the  $\text{WS}_2\text{-WS}_{2(1-x)}\text{Se}_{2x}$  dataset and 40-200 mrad for the graphene dataset.

### *Sample Preparation*

Synthesis of twisted bilayer graphene was prepared following the procedure outlined in Wang et al.<sup>34</sup> This involved the direct transfer of chemical vapor deposition (CVD)-synthesized graphene from Cu foil onto a holey carbon covered TEM grid, followed by precleaning in ambient air at 250 °C. The sample was then exposed to air of near-saturation humidity overnight. Once in the microscope, the sample was further cleaned by a 30-minute beam shower, achieving a level of cleanness that allows a very intense STEM probe to operate continuously for hours without

electron-beam induced deposition of hydrocarbons<sup>34</sup>. The bilayer region shown was formed either during the graphene CVD growth or as a result of accidental fold-over during the transfer process.

The twisted WS<sub>2</sub> bilayer samples were prepared by stacking two MOCVD grown WS<sub>2</sub> monolayers using a wet transfer method as described in Wang et al.<sup>35</sup> This twisted WS<sub>2</sub> bilayer was then implanted with Se atoms using a maximum kinetic energy of ~8.5 eV/atom via PLD to form fractional Janus WSSe on the exposed monolayer, resulting in WS<sub>2</sub>-WS<sub>2(1-x)</sub>Se<sub>2x</sub>. Full details of the Se implantation can be found in Lin et al.<sup>23</sup> and Harris et al.<sup>24</sup>

### *Kernel Density Estimate Bootstrapping*

The bandwidth parameter, was set to 0.1, chosen by Silverman's rule of thumb to balance bias and variance in the density estimates. To quantify the uncertainty in our KDE estimates, we employed a bootstrapping approach. We generated 1000 bootstrap samples by resampling the original dataset with replacement, each containing the same number of data points as the original dataset. For each bootstrap sample, we computed the KDE using the same parameters as described above. The mean and standard deviation of the KDE values were then calculated across the 1000 bootstrap samples.

### **Data availability**

The data that support the findings of this study are openly available at:

<https://drive.google.com/drive/folders/1tDF283xry5op3t594oBUlcNLKbjRTV7C?usp=sharing>

### **Code availability**

The code for this study can be accessed via this link: <https://github.com/ahoust17/Gomb-Net.git>

### **Acknowledgements**

This work was supported by the U.S. Department of Energy, Office of Science, Basic Energy Sciences, Materials Sciences and Engineering Division. Development of machine learning methods was supported by the Center for Nanophase Materials Sciences (CNMS), which is a U.S. Department of Energy, Office of Science User Facility at Oak Ridge National Laboratory.

The microscopy and machine learning in this work was partially supported by the AI Tennessee Initiative and the Electron Microscopy Center at the University of Tennessee, Knoxville. For the MOCVD growth of 2D WS<sub>2</sub> crystals Y.-C. L. acknowledges funding from NEWLIMITS, a center in nCORE as part of the Semiconductor Research Corporation (SRC) program sponsored by NIST through award number 70NANB17H041.

## **Author Declarations**

### *Conflict of Interest:*

The authors have no conflicts to disclose.

### *Author Contributions:*

**ACH:** Conceptualization (equal); writing—original draft (lead); writing—review & editing (equal); data curation (equal); methodology (equal); software (lead); visualization (lead). Investigation (lead). **SBH:** Conceptualization (equal); writing—original draft (supporting); writing—review & editing (equal); data curation (equal); methodology (equal); software (supporting); Investigation (supporting). **HW:** Investigation (supporting). **Y-CL:** Investigation (supporting). **DGB:** Resources (equal); Writing – review & editing (equal). **KX:** Funding acquisition (lead); Resources (equal); Writing – review & editing (equal). **GD** Resources (equal); Writing – review & editing (equal).

## References:

1. Kennes, D. M. et al. Moiré heterostructures as a condensed-matter quantum simulator. *Nature Physics* 17:2 17, 155–163 (2021).
2. Nuckolls, K. P. & Yazdani, A. A microscopic perspective on moiré materials. *Nature Reviews Materials* 9:7 9, 460–480 (2024).
3. Yu, H., Liu, G. Bin, Tang, J., Xu, X. & Yao, W. Moiré excitons: From programmable quantum emitter arrays to spin-orbit-coupled artificial lattices. *Sci Adv* 3, (2017).
4. Bistritzer, R. & MacDonald, A. H. Moiré bands in twisted double-layer graphene. *Proc Natl Acad Sci U S A* 108, 12233–12237 (2011).
5. Ziatdinov, M., Ghosh, A., Wong, C. Y. & Kalinin, S. V. AtomAI framework for deep learning analysis of image and spectroscopy data in electron and scanning probe microscopy. *Nature Machine Intelligence* 4:12 4, 1101–1112 (2022).
6. Lin, R., Zhang, R., Wang, C., Yang, X. Q. & Xin, H. L. TEMImageNet training library and AtomSegNet deep-learning models for high-precision atom segmentation, localization, denoising, and deblurring of atomic-resolution images. *Scientific Reports* 11:1 11, 1–15 (2021).
7. Kalinin, S. V. et al. Machine learning in scanning transmission electron microscopy. *Nature Reviews Methods Primers* 2:1 2, 1–28 (2022).
8. Lee, C. H. et al. Deep learning enabled strain mapping of single-atom defects in two-dimensional transition metal dichalcogenides with sub-picometer precision. *Nano Lett*, 3369–3377 (2020).
9. Ziatdinov, M. et al. Deep Learning of Atomically Resolved Scanning Transmission Electron Microscopy Images: Chemical Identification and Tracking Local Transformations. *ACS Nano* 11, 12742–12752 (2017).
10. Ni, H. et al. Quantifying Atomically Dispersed Catalysts Using Deep Learning Assisted Microscopy. *Nano Lett*, 7442–7448 (2023).
11. Vasudevan, R. K. et al. Mapping mesoscopic phase evolution during E-beam induced transformations via deep learning of atomically resolved images. *npj Computational Materials* 4:1 4, 1–9 (2018).
12. Ghosh, A., Sumpter, B. G., Dyck, O., Kalinin, S. V. & Ziatdinov, M. Ensemble learning-iterative training machine learning for uncertainty quantification and automated experiment in atom-resolved microscopy. *npj Computational Materials* 7:1 7, 1–8 (2021).
13. Ronneberger, O., Fischer, P. & Brox, T. U-Net: Convolutional Networks for Biomedical Image Segmentation. *ArXiv* (2015).
14. Minaee, S. et al. Image Segmentation Using Deep Learning: A Survey. *IEEE Trans Pattern Anal Mach Intell* 44, 3523–3542 (2022).
15. Rakib, T., Pochet, P., Ertekin, E. & Johnson, H. T. Moiré engineering in van der Waals heterostructures. *J Appl Phys* 132, 120901 (2022).
16. Jiang, J., Xu, T., Lu, J., Sun, L. & Ni, Z. Defect Engineering in 2D Materials: Precise Manipulation and Improved Functionalities. *Research*, (2019).

17. Rhodes, D., Chae, S. H., Ribeiro-Palau, R. & Hone, J. Disorder in van der Waals heterostructures of 2D materials. *Nature Materials* 18:6 18, 541–549 (2019).
18. He, Y. M. et al. Single quantum emitters in monolayer semiconductors. *Nature Nanotechnology* 10:6 10, 497–502 (2015).
19. Mahbod, A. et al. A dual decoder U-Net-based model for nuclei instance segmentation in hematoxylin and eosin-stained histological images. *Front Med* 9, 978146 (2022).
20. Castro Neto, A. H., Guinea, F., Peres, N. M. R., Novoselov, K. S. & Geim, A. K. The electronic properties of graphene. *Rev Mod Phys* 81, 109–162 (2009).
21. de Jong, T. A. et al. Imaging moiré deformation and dynamics in twisted bilayer graphene. *Nature Communications* 13:1 13, 1–8 (2022).
22. Geohegan, D. B., Poretzky, A. A. & Xiao, K. Growing tunable moiré matter. *Nature Materials* 23:3 23, 308–309 (2023).
23. Lin, Y. C. et al. Low Energy Implantation into Transition-Metal Dichalcogenide Monolayers to Form Janus Structures. *ACS Nano* 14, 3896–3906 (2020).
24. Harris, S. B. et al. Real-Time Diagnostics of 2D Crystal Transformations by Pulsed Laser Deposition: Controlled Synthesis of Janus WSSe Monolayers and Alloys. *ACS Nano* 17, 2472–2486 (2023).
25. Lu, A. Y. et al. Janus monolayers of transition metal dichalcogenides. *Nature Nanotechnology* 12:8 12, 744–749 (2017).
26. Tan, H. J. et al. Crucial Role of Crystal Field on Determining the Evolution Process of Janus MoSSe Monolayer: A First-Principles Study. *Journal of Physical Chemistry Letters* 13, 9287–9294 (2022).
27. Maity, I., Maiti, P. K., Krishnamurthy, H. R. & Jain, M. Reconstruction of moiré lattices in twisted transition metal dichalcogenide bilayers. *Phys Rev B* 103, L121102 (2021).
28. Hjorth Larsen, A. et al. The atomic simulation environment—a Python library for working with atoms. *Journal of Physics: Condensed Matter* 29, 273002 (2017).
29. Maas, A. L., Hannun, A. Y. & Ng, A. Y. Rectifier Nonlinearities Improve Neural Network Acoustic Models. (2013).
30. Kingma, D. P. & Ba, J. L. Adam: A Method for Stochastic Optimization. 3rd International Conference on Learning Representations, ICLR 2015 - Conference Track Proceedings (2014).
31. Liaw, R. et al. Tune: A Research Platform for Distributed Model Selection and Training. (2018).
32. Akiba, T., Sano, S., Yanase, T., Ohta, T. & Koyama, M. Optuna: A Next-generation Hyperparameter Optimization Framework. *Proceedings of the ACM SIGKDD International Conference on Knowledge Discovery and Data Mining* 2623–2631 (2019) doi:10.1145/3292500.3330701.
33. Sudre, C. H., Li, W., Vercauteren, T., Ourselin, S. & Jorge Cardoso, M. Generalized Dice Overlap as a Deep Learning Loss Function for Highly Unbalanced Segmentations. *Lecture*

- Notes in Computer Science (including subseries Lecture Notes in Artificial Intelligence and Lecture Notes in Bioinformatics) 10553 LNCS, 240–248 (2017).
34. Wang, H., Randeniya, M., Houston, A., Duscher, G. & Gu, G. Ultraclean Suspended Graphene by Radiolysis of Adsorbed Water. *Nano Lett* (2024)
  35. Wang, K. et al. Interlayer Coupling in Twisted WSe<sub>2</sub>/WS<sub>2</sub> Bilayer Heterostructures Revealed by Optical Spectroscopy. *ACS Nano* 10, 6612–6622 (2016).